

Statement

This manuscript is a non-peer reviewed preprint posted to EarthArxiv. The manuscript was submitted to Geophysical Journal International on 6 September 2021, and subsequent versions may have slightly different content. If accepted, the final version of this manuscript will be available via the 'Peer-reviewed Publication DOI' link on the right-hand side of this webpage. Please feel free to contact any of the authors; we welcome feedback.

1 **Structural controls on earthquake rupture revealed by the 2020**
2 **M_w 6.0 Jiashi earthquake (Kepingtag belt, SW Tian Shan,**
3 **China)**

4 Siyu Wang^{1*}, Edwin Nissen¹, Léa Pousse-Beltran^{1,2}, Tim J. Craig³, Ruohong Jiao¹,
and Eric A. Bergman⁴

¹*School of Earth and Ocean Sciences, University of Victoria, Victoria V8P 5C2, British Columbia, Canada*

²*Institute des Sciences de la Terre, Université Grenoble Alpes, 38058 Grenoble, France*

³*School of Earth and Environment, COMET, Institute of Geophysics and Tectonics, University of Leeds, Leeds, UK*

⁴*Global Seismological Services, Golden, CO 80401, USA*

5 6 September 2021

6 **SUMMARY**

7 The Kepingtag (Kalpin) fold-and-thrust belt of the southern Chinese Tian Shan is character-
8 ized by active shortening and intense seismic activity. Geological cross-sections and seismic
9 reflection profiles suggest thin-skinned, northward-dipping thrust sheets detached in an Upper
10 Cambrian décollement. The January 19 2020 M_w 6.0 Jiashi earthquake provides an oppor-
11 tunity to investigate how coseismic deformation is accommodated in this structural setting.
12 Coseismic surface deformation resolved with Sentinel-1 Interferometric Synthetic Aperture
13 Radar (InSAR) is centered on the back limb of the frontal Kepingtag anticline. Elastic dis-
14 location modelling suggests that the causative fault is located at ~ 7 km depth and dips $\sim 7^\circ$
15 northward, consistent with the inferred position of the décollement. The narrow slip pattern
16 (length ~ 37 km but width only ~ 9 km) implies that there is a strong structural or litholog-
17 ical control on the rupture extent, with up-dip slip propagation possibly halted by an abrupt

18 change in dip angle where the Kepingtag thrust is inferred to branch off the décollement. A
19 depth discrepancy between mainshock slip constrained by InSAR and teleseismic waveform
20 modelling (~ 7 km) and well-relocated aftershocks (~ 10 – 20 km) may imply that sediments
21 above the décollement are velocity strengthening. We also relocate 148 regional events from
22 1977 to 2020 to characterize the broader distribution of seismicity across the Kepingtag belt.
23 The calibrated hypocenters combined with previous teleseismic waveform models show that
24 thrust and reverse faulting earthquakes cluster at relatively shallow depths of ~ 7 – 15 km but
25 include abundant out-of-sequence events both north and south of the frontal Kepingtag fault.

26 **Key words:** Radar interferometry, Asia, Earthquake source observations, Waveform inversion,
27 Folds and folding, Intra-plate processes

28 1 INTRODUCTION

29 Late Cenozoic crustal deformation in central Asia is dominated by reverse and strike-slip faulting
30 and folding within and around the margins of the Tian Shan mountains. Geodetic data indicate
31 that ~ 6 – 9 mm/yr of the present-day shortening occurs across the Chinese Tian Shan between the
32 northwestern Tarim Basin and southern Kyrgyzstan (Reigber et al., 2001). The Kepingtag (Kalpin)
33 fold-and-thrust belt has developed along part of the southern margin of this range (Fig. 1). This
34 actively-deforming belt is one of the most earthquake-prone regions of the Tian Shan and of China.
35 In recent years, this intense seismicity has attracted much interest in the deformation style, rate
36 and other characteristics of the Kepingtag belt (Allen et al., 1999; Zhou & Xu, 2000; Zhang et al.,
37 2008; Yang et al., 2002, 2006; Ran et al., 2006). Furthermore, it is one of the few parts of Tian
38 Shan where deformation can be seen stepping into the surrounding foreland, with emergent thrust
39 sheets predominantly vergent toward the Tarim basin in the south. Therefore, the deformation of
40 the Kepingtag belt can also inform how the mountain ranges of southern Tian Shan grow through
41 time.

42 Fold-and-thrust belts pose distinct challenges for seismic hazard assessment since much of the
43 active faulting is buried. This is exemplified by iconic earthquakes such as the 1978 M_s 7.4 Tabas,

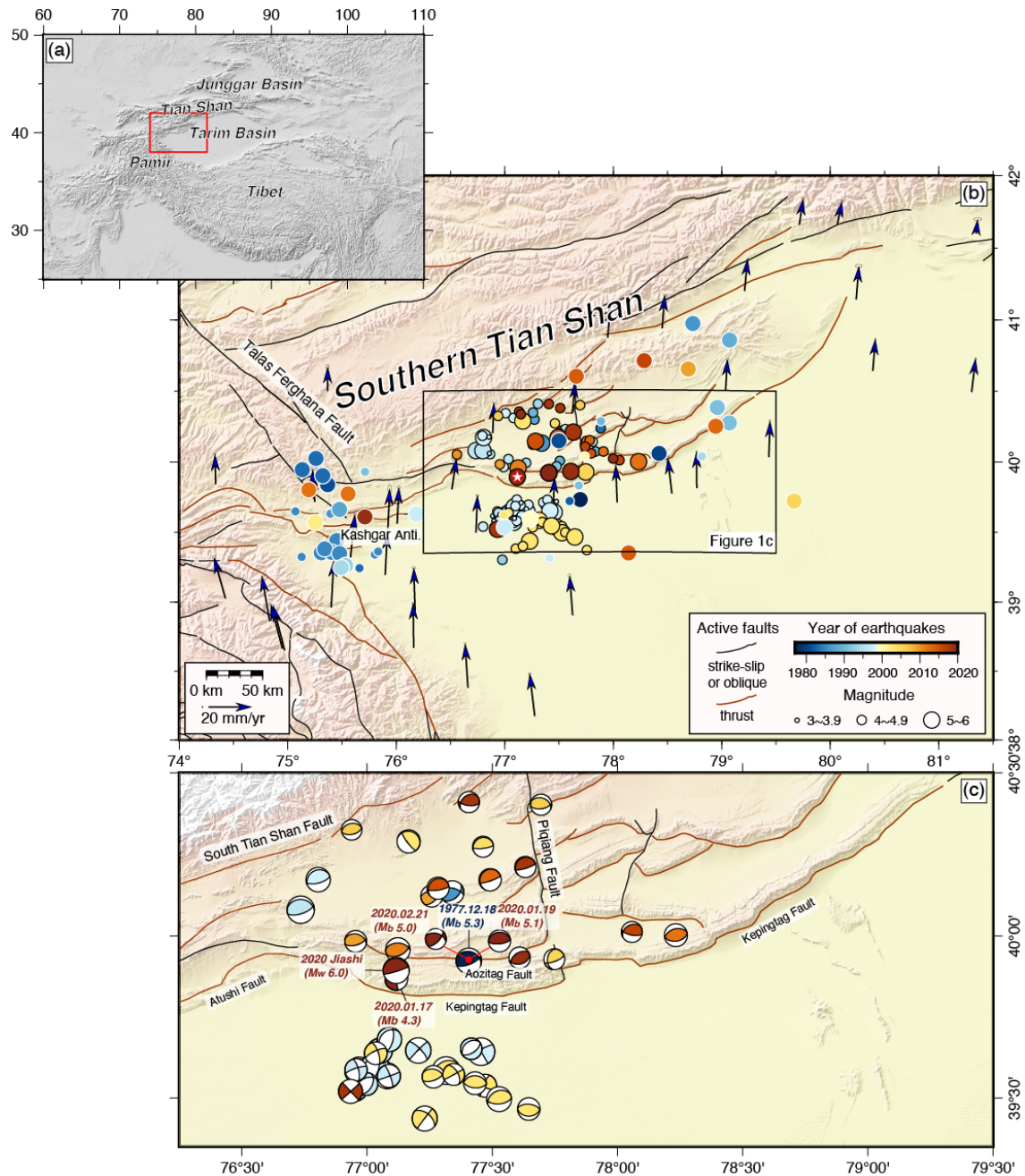


Figure 1. Tectonics and seismicity of the study area. (a) Shaded relief of the Himalayan orogeny with the location of panel (b) outlined in red. (b) Tectonic map of the southern Tian Shan. Instrumental seismicity is scaled by magnitude and colored by year from 1977.12.18 to 2020.02.21. Our own relocated epicenters are shown with black outlines, while those from the United States Geological Survey (USGS) have white outlines. The white star is the relocated epicenter of the 2020 January 19 Jiashi mainshock. Active faults are from the online database provided by the Institute of Geology, China Earthquake Administration (<http://www.neotectonics.cn/arcgis/apps/webappviewer/index.html?id=3c0d8234c1dc43eaa0bec3ea03bb00bc>) and Global Navigation Satellite Systems (GNSS) velocities relative to stable Eurasia are from Wang et al. (2020). (c) Topography, active faults, and earthquakes of the Kepingtag fold-and-thrust belt. Focal mechanisms are from teleseismic body-waveform modelling studies or the Global Centroid Moment Tensor (CGMT) catalog (see Table 1 for details). They are plotted at our relocated epicenters, coloured by year and scaled by magnitude.

44 Iran earthquake (Walker et al., 2003) and the 1987 M_w 5.9 Whittier and 1994 M_w 6.7 Northridge,
45 California earthquakes (e.g., Davis et al., 1989; Jones et al., 1994), each characterized by shallow
46 folding and blind faulting without accompanying surface rupture. There are many other examples
47 of large earthquakes that ruptured faults were not previously mapped, and where historical and
48 instrumental records were too short to have revealed the associated seismic hazard beforehand.
49 Furthermore, fold-and-thrust belts contain a wide range of fault structures including décollements
50 and ramp-and-flat thrusts, and it is often not clear which of these host large earthquakes and which
51 creep aseismically (e.g., Copley, 2014; Ainscoe et al., 2017; Mallick et al., 2021). It is also impor-
52 tant to consider how subsurface structure and stratigraphy may influence rupture extents, and thus
53 potential earthquake magnitudes (e.g., Elliott et al., 2011; Nissen et al., 2011).

54 On January 19 2020 at 13:27:56 UTC, a M_w 6.0 earthquake struck near Jiashi in the west-
55 ern Kepingtag belt ($\sim 39.83^\circ\text{N}$, 77.21°E) (Fig. 1), causing intense ground shaking and damage
56 to hundreds of buildings. A regional seismic network recorded 1,639 aftershocks as of Febru-
57 ary 11 2020 (Ran et al., 2020), with the largest (M_b 5.1) occurring ~ 1 hour after the mainshock.
58 This sequence provides an opportunity to investigate patterns of seismicity and deformation in this
59 region. Routine teleseismic moment tensor solutions for the mainshock from the U.S. Geological
60 Survey (USGS) and the Global Centroid Moment Tensor project (GCMT) implicate thrust or re-
61 verse faulting, but exhibit discrepancies of tens of degrees in strike, dip, and rake and of several
62 kilometers in centroid depth and location. This makes it difficult to associate the earthquake with
63 specific faulting or characterize its tectonic implications without further investigation (Engdahl
64 et al., 2006; Weston et al., 2011; Wimpenny & Scott Watson, 2020).

65 Fortunately, Interferometric Synthetic Aperture Radar (InSAR) observations and modelling
66 can provide more precise constraints on fault geometries and depth extents of large, shallow conti-
67 nental earthquakes (e.g., Elliott et al., 2016). Furthermore, growing compilations of seismic phase
68 arrival times can help relocate earthquake hypocenters more accurately which, in conjunction with
69 InSAR slip models, can provide additional information on rupture directivity (e.g., Pousse-Beltran
70 et al., 2020). In this paper, we map the surface deformation of the 2020 Jiashi earthquake using the
71 Sentinel-1 InSAR imagery and characterize its subsurface fault geometry and slip distribution us-

ing elastic dislocation modelling. We provide an independent check on its mechanism and centroid depth using teleseismic body waveform modelling and pinpoint its hypocenter using a calibrated, multi-event relocation. We relate some striking features of the surface deformation and slip model to the subsurface structure of the Kepingtag belt. Our multi-event relocation also allows us to reassess earlier instrumental earthquakes in this region. These new results are used to reevaluate the active tectonics and seismic hazard of the Kepingtag belt.

2 TECTONIC SETTING

The Tian Shan in Central Asia originally formed in the Paleozoic, and most of the present topography of the mountain ranges resulted from Cenozoic reactivation as a result of the India-Eurasia collision (Windley et al., 1990; Hendrix et al., 1992; Avouac & Tapponnier, 1993; Burchfiel et al., 1999). Over time, the deformation has propagated outward into the Tarim and Junggar basins, where along certain parts of the Tian Shan margins, intense folding and faulting have created sets of narrow ridges. The Kepingtag fold-and-thrust belt, located along the arid southern margin of the Chinese Tian Shan, offers one of the clearest examples of this basinward migration of active deformation (Fig. 1b).

2.1 Geology of the Kepingtag belt

About 200 km long by 50 km wide and trending WSW–ENE, the Kepingtag belt consists of fault-related folds associated with a series of south-verging, imbricated thrust stacks (Allen et al., 1999). Folded strata are composed of Cambrian–Ordovician Qiulitag group limestones, Middle Ordovician Saergan group limestone and dolomite, Silurian Kepingtag group sandstone, Devonian sandstone, Carboniferous Kangkelin group sandstone, lower Permian limestone, and Paleogene–Neogene Wuqia group sandstone and conglomerate (Chen et al., 2006; Yang et al., 2010). The thickness of the upper Paleozoic strata in the Kepingtag belt increases from about 2 km in the south to greater than 4 km in the north (Yin et al., 1998). There is a major angular unconformity between the Paleozoic strata and the Cenozoic foreland basin deposits, with the near absence of Mesozoic sedimentary rocks implying significant Paleozoic crustal shortening.

Table 1. Earthquake source parameters in the Kepingtag belt and its foreland. Relocated hypocenters are from this study. The focal depth (FD) is followed by a superscript letter describing how it was calibrated: *d* = teleseismic depth phases, *l* = local-distance readings, *n* = near-source station readings, and *c* = cluster default depths. Focal mechanisms are taken from (1) Fan et al. (1994), (2) Sloan et al. (2011), (3) Ghose et al. (1998), (4) the Global Centroid Moment Tensor (GCMT) catalogue, and (5) this study. The centroid depth (CD) is also given a superscript letter that describes whether it was obtained by modelling (*t*) teleseismic body-waveforms, (*d*) teleseismic depth phases, (*r*) regional waveforms, or (*i*) = InSAR surface displacements. Where only a less reliable GCMT centroid depth is available, we mark the solution with an asterisk.

Date	Time	Relocated hypocenter			Focal mechanism				M_w	Ref.
		Long.	Lat.	FD (km)	CD (km)	Strike	Dip	Rake		
1977.12.18	16:47	77.4065	39.9236	22 ^d	7 ^t	74	51	79	5.8	1
1986.04.25	16:12	77.3404	40.1340	13 ^d	15*	283	60	125	5.4	4
1996.03.19	15:00	76.7353	40.0810	13 ^l	34 ^t	234	16	87	6.0	2
1996.03.20	00:14	76.8644	40.0562	17 ^l	6 ^r	268	20	76	4.5	3
1996.03.22	08:26	76.7983	40.0816	15 ^l	6 ^r	260	18	78	5.2	3
1996.04.02	02:28	77.5587	40.2328	10 ^l	16 ^r	242	59	128	4.1	3
1997.01.21	01:48	77.2050	39.6475	11 ^l	12 ^t	317	85	177	5.4	2
1997.01.29	08:20	76.9678	39.5923	12 ^l	33*	04	83	132	5.2	4
1997.03.01	06:04	76.9532	39.5288	14 ^l	14 ^d	180	80	-173	5.6	2,4
1997.04.05	23:36	76.9622	39.5832	12 ^l	18 ^t	177	64	-139	5.4	2
1997.04.06	04:36	77.0809	39.5694	12 ^l	17 ^t	246	41	-74	5.8	2
1997.04.06	12:58	77.0324	39.6105	17 ^l	13 ^t	210	38	-74	5.1	2
1997.04.11	05:34	77.0326	39.6023	15 ⁿ	20 ^t	226	42	-79	6.0	2
1997.04.12	21:09	77.0039	39.5334	14 ⁿ	16 ^t	239	27	-74	5.1	2
1997.04.15	18:19	77.0506	39.6461	14 ⁿ	18 ^t	177	64	-139	5.7	2
1997.06.24	09:24	76.9562	39.5877	16 ⁿ	34*	345	72	-167	5.1	4
1997.10.17	17:35	77.0875	39.5686	25 ^d	33*	177	64	-139	5.3	4
1998.03.19	13:51	76.8048	40.1732	15 ^l	15 ^d	243	5	79	5.6	2,4
1998.08.02	04:40	77.0897	39.6817	10 ^d	15 ^t	173	40	-140	5.5	2
1998.08.03	15:15	77.0905	39.6527	15 ^l	29 ^r	253	10	129	4.6	2
1998.08.27	09:03	77.4554	39.6437	16 ^l	15 ^t	57	80	1	6.3	2
1998.09.03	06:43	77.4162	39.6528	25 ^d	10 ^r	179	59	178	4.8	2
1998.10.31	16:09	77.2469	39.6081	19 ^l	14 ^r	152	74	-164	4.6	2
2003.01.04	11:07	77.0350	39.6389	14 ^l	33*	245	73	-20	5.2	4
2003.02.24	02:03	77.3157	39.5852	19 ^l	5 ^t	280	17	115	6.2	2
2003.02.24	21:18	77.2653	39.5663	12 ^l	15*	289	33	126	5.2	4
2003.02.25	03:52	77.4717	39.5385	8 ^l	15*	239	33	62	5.3	4
2003.03.12	04:47	77.5273	39.4969	8 ^l	7 ^d	245	33	73	5.7	2,4
2003.03.15	22:59	77.3459	39.5733	9 ^l	15*	330	57	178	5.0	4
2003.03.30	23:15	77.4315	39.5462	17 ^l	10 ^t	287	27	117	5.2	2
2003.05.04	15:44	77.2305	39.4369	9 ^l	15*	308	53	179	5.8	4
2003.06.04	16:28	77.6458	39.4665	10 ^l	10 ^d	274	54	92	5.2	2,4
2003.09.26	23:35	77.1664	40.2902	30 ^d	15*	290	13	58	5.3	4
2004.10.07	16:14	77.4633	40.2740	12 ^l	17*	245	14	72	4.8	4
2005.03.24	07:37	77.7478	39.9288	11 ^d	30*	187	35	32	4.8	4
2006.06.08	11:34	77.6951	40.4025	6 ^d	30*	290	35	113	4.8	4
2006.09.06	07:51	76.9389	40.3257	15 ^l	32*	258	37	91	4.7	4
2009.04.22	09:26	77.2583	40.1229	11 ^d	16*	264	50	124	5.0	4
2009.10.16	02:56	76.9545	39.9836	15 ^d	19*	284	32	116	5.0	4
2011.08.11	10:06	77.1232	39.9575	19 ^d	12*	272	42	109	5.6	4
2012.08.11	09:34	78.2335	40.0027	15 ^d	12*	255	43	84	5.3	4
2013.03.11	03:01	77.4916	40.1729	9 ^d	12*	210	11	50	5.2	4
2015.01.10	06:50	77.2838	40.1469	14 ^c	15*	227	17	57	5.1	4
2016.07.09	16:36	78.0578	40.0128	14 ^c	12*	240	32	53	4.8	4
2018.04.12	10:41	77.4068	40.4104	17 ^l	22*	231	36	50	4.9	4
2018.09.03	21:52	76.9341	39.5211	14 ^c	15*	317	89	178	5.5	4
2018.11.03	21:36	77.6323	40.2120	14 ^c	12*	225	12	63	4.9	4
2019.01.06	16:22	77.6093	39.9331	6 ^d	12*	238	50	79	4.9	4
2020.01.17	16:05	77.1167	39.8682	12 ^d	21*	261	86	-178	5.3	4
2020.01.19	13:27	77.1161	39.8944	11 ^d	7 ⁱ	279	7	115	6.0	5
2020.01.19	14:23	77.4089	39.9236	14 ^c	18*	268	22	95	5.1	4
2020.02.21	15:39	77.4059	39.9232	14 ^c	14*	287	46	143	4.8	4

98 The thick Paleozoic sequence of mainly Upper Cambrian to Permian strata is exposed in
99 a series of parallel anticlines (Xinjiang Bureau of Geology and Mineral Resources, 1992). The
100 hanging wall cut-offs of the imbricate thrusts have been eroded away. This thrust system is inter-
101 preted as thin-skinned, with fault-propagation folds detached in Upper Cambrian limestones along
102 a décollement at $\sim 6\text{--}10$ km depth according to seismic reflection profiles and balanced geological
103 cross-sections (Allen et al., 1999; Yin et al., 1998; Nishidai & Berry, 1990; Yang et al., 2010).
104 The left-lateral Piqiang fault (Fig. 1) has developed perpendicular to the Kepingtag belt, dividing
105 it into two (western and eastern) segments. Interpretations of satellite imagery and balanced cross-
106 sections suggest that the thin-skinned imbricate thrusting and folding has accommodated crustal
107 shortening strains of 20–28% between the main Tian Shan and Tarim block, equivalent to ~ 35 km
108 across the western segment and ~ 22 km across the eastern segment (Allen et al., 1999; Yin et al.,
109 1998).

110 **2.2 Seismicity of the Kepingtag belt**

111 Active crustal shortening and thickening of the southern Tian Shan is manifest in frequent reverse
112 faulting earthquakes that cluster around the margins of the high topography with nodal planes ori-
113 ented approximately parallel to the range (Ghose et al., 1998; Xu et al., 2006; Sloan et al., 2011).
114 The Kepingtag belt and its adjacent foreland are amongst the most seismically-active parts of the
115 Tian Shan, with thirty-six earthquakes of M_w 5.0–6.3 since the late 1970s (Fig. 1b and Table 1).
116 The 1902 M_w 7.7 Atushi (Kashgar) earthquake, located ~ 150 km west of our study area, hints
117 that much larger earthquakes may be possible (Kulikova & Krüger, 2017). Within the Keping-
118 tag belt, instrumental seismicity is concentrated west of the Piqiang fault and the available focal
119 mechanisms indicate a predominance of thrust and reverse faulting. Assuming that northward-
120 dipping nodal planes represent faulting, dip angles range from $\sim 5^\circ\text{--}60^\circ$ with an average of around
121 30° . Only a few of these events have reliable centroid depths from detailed waveform modelling,
122 mostly in the range 6–16 km, consistent with faulting within the lower sedimentary cover and the
123 underlying basement (Fan et al., 1994; Ghose et al., 1998; Sloan et al., 2011). Sloan et al. (2011)
124 placed a single outlier event at 34 km depth, within the middle-to-lower crust, but noted that its

125 relatively complex waveforms could potentially be explained by a compound (multi-event) source
126 mechanism at a much shallower depth.

127 Seismicity in our study area peaked between 1997 and 1998 with thirteen earthquakes of
128 M_w 5.0–6.3 including the destructive January–October 1997 Jiashi earthquake swarm in the fore-
129 land south of the Kepingtag belt, which caused 21 fatalities (Zhang et al., 1999). This sequence
130 involved a mix of strike-slip and normal faulting with well-resolved centroid depths of ~ 12 – 20 km
131 (Sloan et al., 2011), as well as some smaller, deeper earthquakes located by a temporary regional
132 network but without reliable focal mechanisms (Xu et al., 2006). The mechanisms and depths are
133 challenging to interpret but may reflect flexural rebound of the Tarim basin under loading from the
134 Tian Shan (Sloan et al., 2011). On February 24 2003, a M_w 6.2 earthquake struck the same area,
135 resulting in 261 reported fatalities. In contrast with the 1997 swarm, the 2003 earthquake involved
136 northward-dipping thrust faulting with a much shallower centroid depth of ~ 5 – 7 km, interpreted
137 to represent southward propagation of the Kepingtag belt into the Tarim basin (Sloan et al., 2011).
138 It also produced an abundant aftershock sequence that was apparently concentrated in the middle
139 crust between ~ 15 – 25 km (Huang et al., 2006). Following the 2003 sequence, the study area en-
140 tered a relatively quiescent period of seismic activity, with no earthquake of magnitude 6 or above
141 until the January 19 2020 event.

142 The 2020 Jiashi sequence occurred within the southern part of the western Kepingtag belt. The
143 M_w 6.0 mainshock was preceded by two days of foreshock activity involving \sim N–S-oriented left-
144 lateral strike-slip faulting (Yao et al., 2021a). The mainshock itself ruptured an \sim E–W-oriented
145 thrust or reverse fault, though there is disagreement amongst available seismological and geodetic
146 models on its geometry and depth, which will be discussed further in light of our own results in
147 Section 4. The mainshock was followed by an energetic aftershock sequence that lasted at least
148 three months (Ran et al., 2020; Yao et al., 2021a). P_g and S_g waves were recorded at fifteen
149 seismic stations, including thirteen permanent stations at ~ 30 – 170 km distance and two local
150 stations ~ 20 km SW and NW of the mainshock epicenter, which were deployed by the Xinjiang
151 Earthquake Administration 4 and 18 hours after the mainshock, respectively. Using P_g and S_g
152 arrival times, hypocenters of the mainshock and ~ 300 $M_L \geq 1.8$ aftershocks up to February 11

153 were relocated using double-differencing (Ran et al., 2020; Yao et al., 2021a). Seismicity forms a
154 ‘T’ shaped pattern in map view, with the mainshock located at the bottom of the ‘T’ and aftershocks
155 extending ~ 20 km northward to the junction of the ‘T’, and from there, ~ 20 km east and west for
156 a total length of ~ 40 km, with the greatest concentration of events along the western branch (Ran
157 et al., 2020; Yao et al., 2021a). These studies also show that the aftershocks are concentrated at
158 depths of 10–20 km.

159 **3 METHODS**

160 **3.1 InSAR measurements**

161 We used InSAR to measure surface deformation in the January 19 2020 earthquake, and elastic
162 dislocation modelling to estimate the fault geometry and slip distribution. The raw data are from
163 the European Space Agency’s C-band Sentinel-1A satellite, with wavelength ~ 5.6 cm. Two as-
164 cending tracks (056A and 129A) and one descending track (034D) capture the Jiashi mainshock.
165 Three, 12 day coseismic interferograms (January 11–23, January 16–28 and January 10–22 2020)
166 were processed using the GAMMA software, and multilooked to 4 looks in range and 20 in az-
167 imuth for a ~ 30 m pixel resolution. The topographic phase contribution was removed using the
168 30 m-resolution Shuttle Radar Topographic Mission Digital Elevation Model, which was also used
169 to geocode the interferograms. The two ascending-track interferograms were unwrapped using the
170 branch-cut algorithm (Goldstein et al., 1988) while the noisier, descending-track interferogram
171 was unwrapped using the Minimum Cost Flow algorithm. Unwrapping errors were then manually
172 corrected.

173 The interferograms exhibit excellent coherence, reflecting the dry desert conditions and sparse
174 vegetation of the southwestern Tian Shan. Coseismic surface deformation is easily distinguished
175 in all three interferograms as a double fringe ellipse elongated in an E-W orientation (Fig. 2a,
176 d, g). The southern lobe is focused on the Kepingtag anticline and exhibits up to ~ 7.5 cm of
177 line-of-sight (LOS) displacement toward the satellite, and the northern lobe is centered along the
178 Aozitag anticline and contains up to ~ 5 cm of displacement away from the satellite (Figure 6a–c).
179 The similarity of the fringe patterns in ascending and descending interferograms implies that the

180 largest contribution to the observed LOS deformation is from uplift/subsidence rather than E/W
181 lateral displacement, consistent with predominantly dip-slip faulting.

182 After downsampling the LOS displacements using a quadtree algorithm to concentrate sam-
183 pling in regions with high phase variance (Jónsson et al., 2002), we employed a two-step inversion
184 strategy to estimate the causative fault parameters. In the first step, we inverted the downsampled
185 data using Powell’s algorithm (Press et al., 1992) and Okada’s expressions (Okada, 1992) to solve
186 for the geometry of a rectangular, uniform slip model fault plane buried in an elastic half space
187 with Lamé parameters $\lambda = \mu = 3.2 \times 10^{10}$ Pa, approximately consistent with regional upper crustal
188 seismic velocities. The single descending interferogram was weighted equal to the two ascending
189 interferograms in the inversion. The optimal model fault strike, dip, rake, length, top and bottom
190 depths, and slip were determined using 500 Monte Carlo restarts with random starting parameters
191 in order to avoid local misfit minima (e.g., Wright et al., 1999). Recognizing a strong trade-off
192 between slip and fault width — which is common for buried thrust earthquakes — we obtained
193 the initial fault geometry by fixing slip to 1.0 m. In the second step, we estimated the slip distri-
194 bution by first extending the uniform slip model fault along strike and up- and down-dip and then
195 dividing the fault plane into $1 \text{ km} \times 1 \text{ km}$ sub-fault patches. We solved for the slip distribution
196 using a finite difference Laplacian constraint to vary smoothing and chose a physically realistic
197 solution using the ‘L-criterion’ (Wright et al., 2004; Funning et al., 2005). We manually removed
198 a few outlier slip patches that lay several kilometers up-dip from the main slip distribution, which
199 we considered spurious. The final distributed slip results were used to generate the forward model
200 and residual interferograms shown in Fig. 2.

201 Given the structural complexity of the Kepingtag belt, we also investigated whether the Jiashi
202 earthquake may have involved non-planar rupture geometries by inverting the InSAR displace-
203 ments for two uniform slip model fault planes (e.g., Pousse-Beltran et al., 2020). We explored a
204 range of listric and anti-listric configurations by matching the top depth of a deeper model fault
205 to the bottom depth of a shallower model fault and varying each of their dip angles at 5° incre-
206 ments. However, none of the two-fault configurations that we tested produced a realistic geometry

207 that improved upon the misfit of the simple, single-fault model. This leads us to strongly favour
208 involvement of a single, planar fault.

209 **3.2 Calibrated hypocenter relocations**

210 We refined the hypocenter of the January 19 2020 mainshock by relocating and calibrating a cluster
211 of regional seismicity using teleseismic, regional and local seismic phase arrival times. In addition
212 to the mainshock, the cluster includes the principal foreshock (m_b 4.3), two largest aftershocks
213 (m_b 5.1 and 5.0), and 148 well-recorded background events starting from 1977. Past multiple-
214 event calibrated relocation studies in comparably instrumented areas elsewhere in Asia indicate
215 that epicenters can be resolved to within $\sim 1\text{--}2$ km and focal depths to within ~ 5 km (Karasözen
216 et al., 2019), improving substantially on the uncertainties of routine catalogs such as the USGS and
217 GCMT (Engdahl et al., 2006). Juxtaposing calibrated epicenters with InSAR-derived slip models
218 can distinguish bilateral from unilateral rupture propagation (e.g., Gaudreau et al., 2019; Pousse-
219 Beltran et al., 2020) and help resolve ambiguities in subsurface fault geometry, which are otherwise
220 commonplace for buried earthquakes (e.g., Roustaei et al., 2010; Copley et al., 2015; Elliott et al.,
221 2015; Karasözen et al., 2018).

222 The cluster was relocated and calibrated in the *Mloc* program using an approach that is fast
223 becoming routine (e.g., Walker et al., 2011; Elliott et al., 2015; Karasözen et al., 2016, 2018, 2019;
224 Gaudreau et al., 2019; Pousse-Beltran et al., 2020; Bergman et al., submitted). *Mloc* utilizes the
225 Hypocentroidal Decomposition method of separating the relocation into two distinct inverse prob-
226 lems reliant on customized phase arrival time data (Jordan & Sverdrup, 1981). In the first step,
227 we solved for the relative locations of each hypocenter with respect to the reference hypocentroid,
228 defined as the arithmetic mean of all individual event hypocenters within the cluster. This step
229 relies principally upon teleseismic arrival times, of which there are an abundance for events in-
230 cluded in the cluster. In the second step we calculated the absolute location of the hypocentroid
231 and updated the absolute hypocenter coordinates of every event in the cluster. For this step we only
232 used seismic phases recorded at local distances of up to 2° , for which there is excellent azimuthal
233 coverage. Using local arrival times for this step is known as ‘direct’ calibration (e.g., Karasözen

et al., 2016). For the best-recorded events, we estimated focal depths using local arrival times; for others, we relied upon teleseismic depth phases or simply fixed the focal depth to a representative cluster default of 14 km. We used a customized velocity model obtained during an earlier calibrated, multi-event relocation performed in the same study area (Bergman et al., submitted).

3.3 Teleseismic body waveform inversion

Finally, we used teleseismic body waveform modelling to provide additional constraints on the mainshock source depth and mechanism, complementing those from InSAR analysis. Centroid depths obtained in this way are particularly useful, since they can help clarify whether fault slip resolved by InSAR models occurred coseismically or through afterslip (Nissen et al., 2014).

We followed the approach of Heimann et al. (2018), and inverted vertical and transverse component data from stations between 3300 and 9900 km from the reported earthquake location. Waveforms were filtered between 0.01 and 1 Hz, and we used a window starting 15 seconds before, and ending 25 seconds after, the principle phase (P for vertical component waveforms, S for transverse component waveforms). Observed data and synthetics were aligned using cross correlation. The Bayesian approach outlined in Heimann et al. (2018) allows for the full sampling of the parameter space available in source depth, latitude, longitude, magnitude, and mechanism. The source-time function is constrained to be a variable-duration half-sinusoid — appropriate for an earthquake of this size, and for the frequencies used in our inversions.

4 RESULTS

Our best-fitting InSAR uniform slip model fault strikes 279° , dips 7° N, has a slight right-lateral component (rake 115°), and is ~ 22 km long by ~ 2 km wide, centered at 7 km depth (Tab. 2). To further test model sensitivity to centroid depth, we ran the inversion by prescribing different (fixed) top and bottom depths while allowing other parameters to vary freely. We also undertook similar tests of model sensitivity to dipping angle. There is a fairly steep increase in misfit at fault center depths shallower or deeper than the minimum misfit value of 7 km (Fig. 3a). For the equivalent

259 dip sensitivity test, we find low misfits for dip angles of 5–10°, but abrupt increases in root mean
260 square error outside of this range.

261 Compared to the uniform slip model, our preferred distributed slip model is longer at ~37 km
262 and wider at ~9 km, but remains centered at ~7 km depth (Fig. 4). The slip distribution is charac-
263 teristically narrow, with an aspect ratio (length to width) of around 4. The peak slip is ~0.5 m and
264 the model moment is $\sim 1.75 \times 10^{18}$ N. The resultant forward model interferogram matches the
265 observed surface deformation closely, with less than one residual fringe and a root mean square
266 error of ~0.25 m (Fig. 2c, f, i), which is substantially lower than that of the uniform slip model
267 (~0.35 m).

268 The fault plane we modelled using InSAR data has a similar strike, dip and rake to the USGS
269 body-wave moment tensor solution, with differences possibly reflecting common trade-offs be-
270 tween strike and rake (Table 2). Our distributed slip model has a slightly larger moment than the
271 three available seismological catalogue solutions. The InSAR data capture the surface deforma-
272 tion accumulated over a period from one week before to one week after the mainshock, and thus
273 it is impossible to separate definitively the mainshock coseismic slip from postseismic motion
274 such as aseismic creep. Therefore, we suggest that the larger moment of our slip model reflects
275 contribution of the postseismic afterslip to the surface deformation.

276 Three other InSAR-derived fault models are also available for comparison (Tab. 2). Our model
277 is closest to the single fault solution of Yu et al. (2020); the two models agree within 4° in strike, dip
278 and rake, and within 1 km in centroid depth. Their preferred, two-fault model is strongly listric,
279 with slip apportioned between a deep, gentle (2°) décollement and a much steeper (52°) ramp.
280 However, we prefer the single-fault solution, as the two-fault models we tested using different
281 configurations of listric and antilistric faults could not yield smaller misfits. Our model is ~2 km
282 deeper and significantly shorter and narrower than a uniform slip model by Yao et al. (2021b).
283 However, they do not provide model or residual interferograms, so there is no easy way to assess
284 the accuracy of their model.

285 Our relocated mainshock hypocenter lies beneath the northern limb of Kepingtag anticline,
286 which is located ~6.6 km NNW from one inferred by Ran et al. (2020) using local data. However,

287 our epicenter is somewhat closer to the InSAR-derived slip distribution patch, lying at its far
288 western end. Both our model and Ran et al. (2020)'s show that the Jiashi earthquake is clearly
289 strongly unilateral, rupturing from west to east. Our relocated epicenter of the January 17, 2020
290 m_b 4.3 foreshock lies ~ 3 km SE from the mainshock, and the two largest aftershocks (m_b 5.1 and
291 5.0) lie near the eastern end of the mainshock model slip patch (Fig. 1c).

292 We show the results of our seismological inversions in Fig. 5 and synthetic waveforms for all
293 stations used in the inversion in the supplementary material (Fig. S1–S4). A probability density
294 function (PDF) of centroid depth results from an inversion with all parameters free shows both the
295 mean and the best-fit solution at just under 10 km (Fig. 5a). Using teleseismic data offers good
296 constraints on the mechanism only near the center of the focal sphere, where the pierce-points of
297 teleseismic waves cluster. As such, the mechanism, and particularly the shallowly dipping nodal
298 plane are poorly constrained (inset mechanism, Fig. 5a). Consequently, we repeated the inversion
299 using double couple nodal planes fixed to match the InSAR-determined fault plane (Fig. 5b). This
300 pushes the PDF slightly deeper, with a mean depth at 11 km, but with a best-fit solution still at
301 10 km, and makes only a marginal difference to the overall misfit values. We also show the PDF
302 for the seismologically-determined magnitude in Fig. 5c, which matches well with the inferred
303 magnitude of the geodetic signal.

304 In order to illustrate the constraints that the teleseismic data offer on the centroid depth, we
305 show a set of six example waveforms (three vertical component, three transverse component) and
306 best-fit synthetics calculated using 3 fixed centroid depths in Fig. 5d. The middle row shows wave-
307 forms calculated at 10 km centroid depth, which is the best fit seismological solution, while the
308 upper row shows waveforms with the depth fixed to match the geodetic results at 7 km, and the
309 lower row shows waveforms with the depth fixed to match the centre of the regionally-determine
310 aftershock distribution at 15 km. We discuss these waveform misfits further in the following sec-
311 tion.

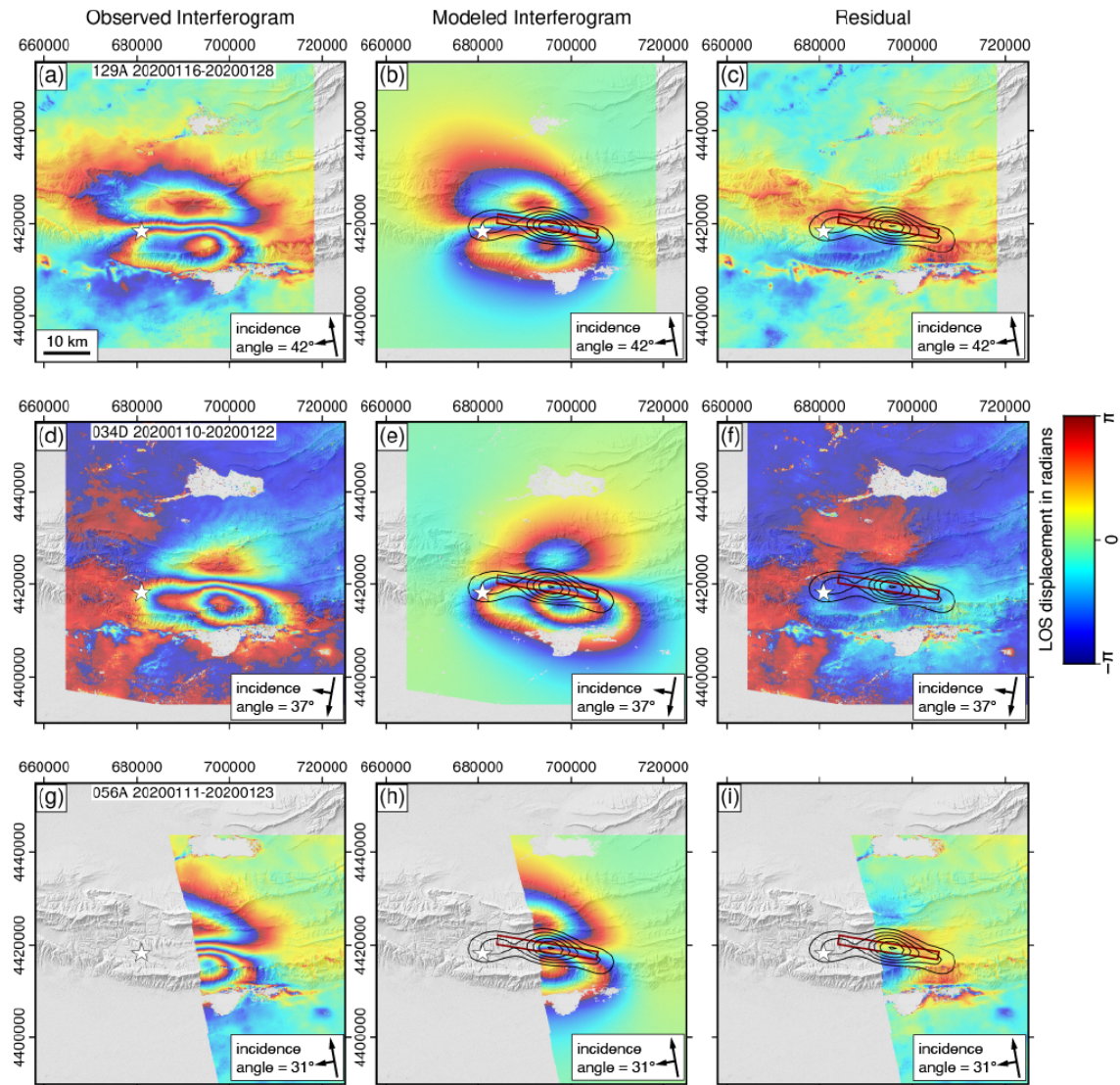


Figure 2. (Left column) Observed, (center) distributed slip model and (right) residual interferograms of the 2020 Jiashi mainshock rupture. Modelling was performed using unwrapped LOS displacements, but the interferograms are re-wrapped to show more clearly the shape of the deformation field. Color cycles of blue through yellow to red indicate motion away from the satellite and one color cycle (2π radians) represents a half radar wavelength (2.77 cm) of LOS displacement. The satellite track azimuths and LOS direction with local angle of incidence are indicated by the longer and shorter black arrows, respectively. The white star indicates the relocated mainshock epicenter. In the central and right-hand panels, ten centimeter model slip contours are shown in black and the outline of the uniform slip model fault plane is marked in dark red.

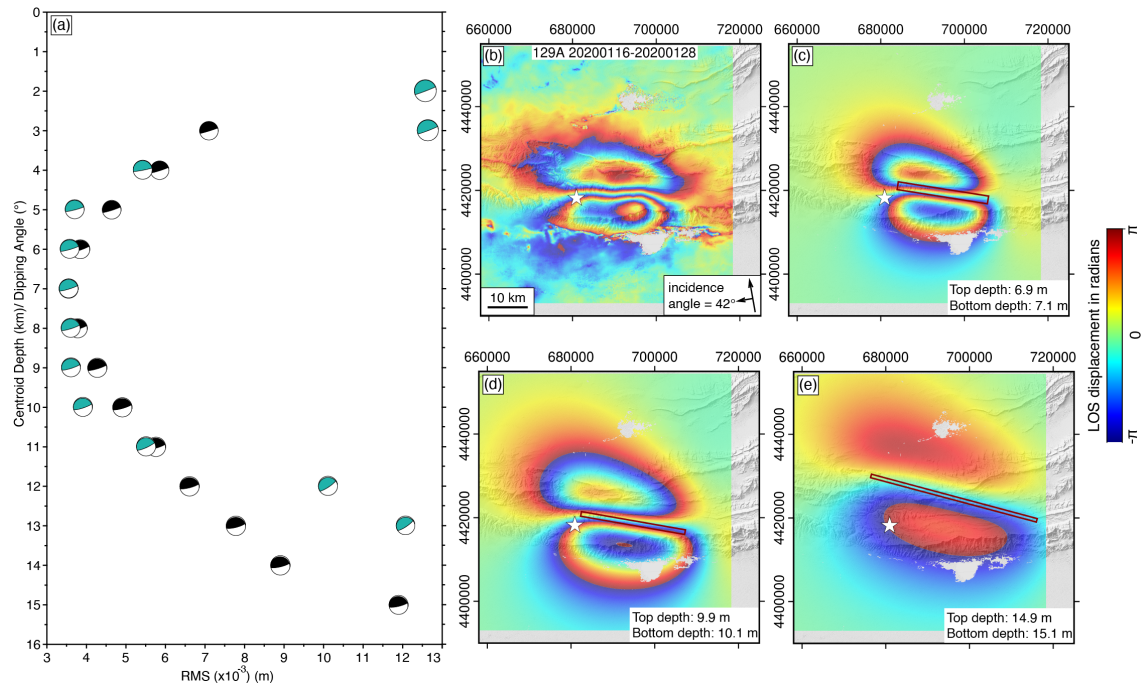


Figure 3. (a) Fault center depth (black) and fault dip (green) sensitivity tests of our InSAR uniform slip fault models for the 2020 Jiashi mainshock. Each focal mechanism shows the minimum-misfit model solution for a fixed center depth (black) or a fixed dip angle (green), with all other parameters kept free in each inversion. The x -axis is root mean square error (RMS) in meters; the y axis shows 1 km increments of fixed center depth and 1° increments of fixed dip. (b) Observed ascending track interferogram (same as in Fig. 2a). (c) Preferred uniform slip model interferogram, with its (free) center depth of 7 km. (d) A forward model interferogram with center depth fixed to 10 km. The forward model used the same uniform slip parameters as in (c) except for the top and bottom depth and the surface projection coordinates. (e) Same as (d) but with a centroid depth of 15 km.

312 5 DISCUSSION

313 5.1 Depth discrepancy between the 2020 Jiashi mainshock and its aftershocks

314 Our InSAR-derived model suggests that the Jiashi mainshock ruptured along the décollement
 315 at the base of the sedimentary cover, with a centroid depth of ~ 7 km. From the high-quality
 316 locally-recorded and double-difference relocated aftershock data, aftershocks cluster along E–W
 317 and NNW–SSE trends, with the former matching the ~ 40 km length and orientation of our slip

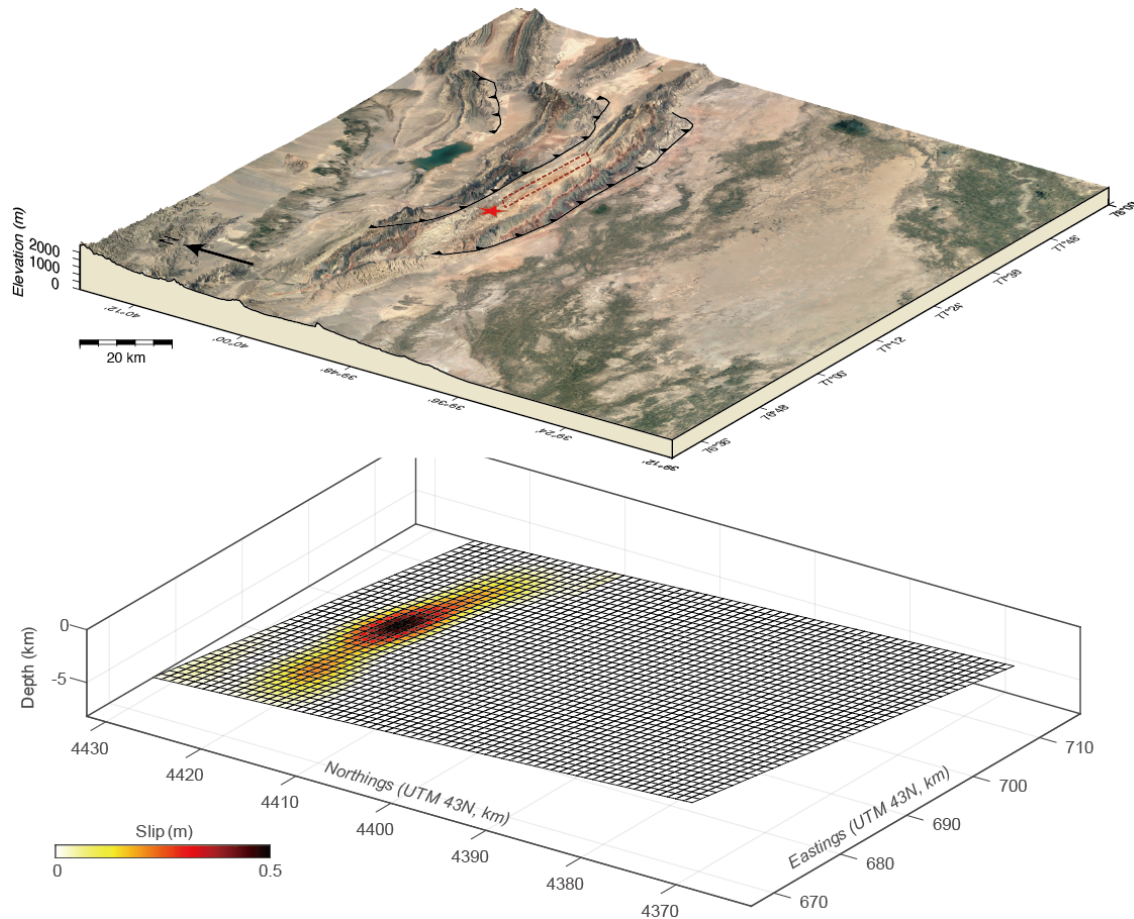


Figure 4. (Top) Google Earth perspective view of the Kepingtag belt and its adjacent foreland. The dark red dashed box marks the outline of our uniform slip model fault plane for the 2020 Jiashi earthquake. The red star is the relocated epicenter near the western end of the fault. (Bottom) Co-located perspective view of the coseismic slip distribution. Significant slip occurs over the depth range 6.5–7.4 km.

318 model (Ran et al., 2020; Yao et al., 2021a). However, locally-recorded aftershocks concentrate
 319 at 10–20 km depth, well below the depth of mainshock slip resolved by InSAR inversion. We
 320 consider two possible explanations for this apparent discrepancy.

321 The first possible explanation is that the surface deformation captured with InSAR may re-
 322 flect aseismic afterslip along the décollement, above an earthquake buried within the underlying
 323 basement and itself invisible to InSAR. We tested this possibility by forward modelling the in-
 324 terferograms based upon a M_w 6.0 thrust earthquake with the same geometry as our preferred

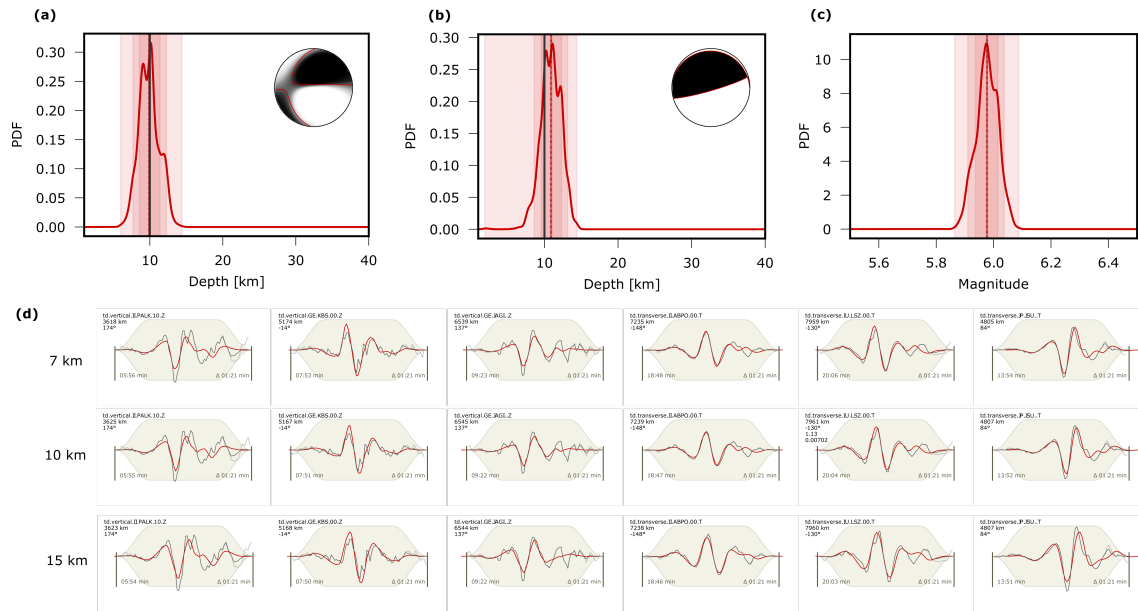


Figure 5. Seismological processing results for the 2020 Jiashi mainshock. (a) Probability-density function for depth, for an inversion with all parameters free. Inset mechanism shows the mechanism probability density function (greys) and the best-fit solution (red). (b) Probability-density function for depth, for an inversion with the mechanism constrained to be a double couple matching the InSAR-derived fault plane. (c) Probability-density function for moment, for an inversion with the mechanism constrained to match the InSAR-derived fault plane. (d) Example waveforms for 6 stations (three vertical component, three transverse component). Black traces show the observed data, red line shows the best-fitting inversion result. Text on each waveform indicates the station and component, epicentral distance, and azimuth. Each row of waveforms show synthetics calculated at 7, 10, and 15 km respectively, as discussed in the text.

325 uniform slip model fault but centered at depths of 10 km and 15 km, more consistent with the
 326 aftershock seismicity (Fig. 3c, d). These forward model interferograms match poorly with the ob-
 327 served InSAR data, with noticeably more far-field deformation and a broader spacing of fringes
 328 between the southern and northern lobes. However, the fact that deformation remains clearly dis-
 329 tinguishable leads us to rule out the possibility that coseismic slip is too deep to be resolved with
 330 InSAR.

331 The second possible explanation is that the InSAR captures mainshock slip but that well-
 332 located aftershocks are vertically separated from the mainshock, faulting within the underly-

Table 2. Source parameters of the 2020 Jiashi mainshock inferred from our model and other sources. The longitude and latitude listed for our InSAR-derived models (first two rows) represent the surface projection of the model slip plane; our relocated epicenter is 77.117° E and 39.894° N. Where three depths are given, they represent the top, middle and bottom depth of the slip plane; where only one is given, it represents the centroid. L and W are length and width, respectively. Yu et al. (2020) prefer their listric, two fault model with a deeper, flatter segment fixed at 2° dip and a shallower, steeper ramp at 52° . Yao et al. (2021b) used uniform slip of 0.32 m in their InSAR-derived model, which may account for their much larger model fault plane.

Source	Long.	Lat.	Strike	Dip	Rake	Depth (km)	L/W (km)	Moment (Nm)	M_w
This study, uniform slip	77.279°	39.902°	279°	7°	115°	7.0/7.1/7.2	22/2	1.31×10^{18}	6.0
This study, distributed slip	77.165°	39.416°	279°	7°	115°	6.3/7.0/7.6	37/9	1.75×10^{18}	6.0
CGMT	77.19°	39.80°	196°	38°	31°	11	–	1.39×10^{18}	6.0
USGS body-wave	77.11°	39.84°	262°	9°	105°	4	–	1.493×10^{18}	6.1
USGS <i>W</i> -phase	77.11°	39.84°	221°	20°	72°	19.5	–	1.387×10^{18}	6.0
Yu et al. (2020), 1 fault	77.30°	39.91°	275°	9°	111°	6.3	–	–	6.1
Yu et al. (2020), 2 faults	77.30°	39.90°	275°	$2^\circ/52^\circ$	111°	4.15	–	–	6.1
Yao et al. (2020)	77.68°	39.31°	269°	20°	92°	4/5/6	58/30	2.29×10^{18}	6.2

ing basement. The absence of shallow aftershocks might reflect that the sediments above the décollement are velocity strengthening (Karasözen et al., 2016), or that the seismic network is insensitive to shallow events due to its average station spacing of ~ 30 km. Local seismic networks are able to constrain the focal depth most accurately only if *Pg* and *Sg* phases are recorded at epicentral distances of less than ~ 1 – 2 times of focal depths and the average station spacing is also less than ~ 1 – 2 times of focal depths (Gomberg et al., 1990). Therefore, the apparent absence of shallow events may be an artefact, as the stations with average spacing of ~ 30 km cannot record aftershocks shallower than 15 km depth.

We prefer the second explanation as the results from teleseismic waveform inversion help us to reinforce that the geodetically-imaged signal is indeed coseismic deformation. The waveform misfit differences between depths of 10 km and 7 km are minimal (Fig. 5d). However, synthetics are notably too broad at all six of the stations shown at depth of 15 km. Due to the cross-correlation based alignment, synthetics are typically aligned on the dominant peak to minimise misfit. However, at 15 km depth, this leads to the peaks to either side being too far out from the main peak

347 due to the increase separation between direct and depth phases. Thus, we conclude that the seis-
348 mological data are consistent with the deformation signal detected using InSAR, but are notably
349 shallower than the aftershocks located using regional seismology.

350 In addition, mainshock–aftershock depth discrepancies are not uncommon and several other
351 earthquake sequences also exhibit similar characteristics. The 2000 M_w 6.6 Torrori (Japan), 2003
352 M_w 6.6 Bam (Iran), 2008 M_w 7.9 Wenchuan (China), 2009 M_w 5.9 Karonga (Malawi), 2011
353 M_w 5.9 Simav (Turkey), and 2014 M_w 6.1 South Napa (California) earthquakes all exhibited
354 shallower mainshock slip, resolved mostly using geodesy, with deeper aftershock distributions,
355 resolved using seismology (Semmane et al., 2005; Jackson et al., 2006; Tong et al., 2010; Wei
356 et al., 2015; Karasözen et al., 2016; Gaherty et al., 2019). Similar patterns were also observed
357 in $M_w \sim 6$ earthquakes and aftershock sequences at Qeshm (2005) and Fin (2006) in the Zagros
358 Simply Folded Belt, Iran (Nissen et al., 2010; Roustaei et al., 2010). These are especially analogous
359 to the Jiashi sequence, as the Zagros mainshocks were centered within a thick sedimentary cover,
360 with aftershock microseismicity vertically separated within the underlying basement (Nissen et al.,
361 2014). Finally, we recollect that the February 24, 2003 M_w 6.2 Jiashi earthquake in the foreland
362 basin south of the Kepingtag was centered at $\sim 5\text{--}7$ km depth, but exhibited aftershocks at $\sim 15\text{--}$
363 25 km depth (Huang et al., 2006; Sloan et al., 2011).

364 **5.2 Structural interpretation of the 2020 Jiashi rupture**

365 Coseismic uplift in the 2020 M_w 6.0 Jiashi earthquake resolved by InSAR is centered along the
366 back limb of the Kepingtag anticline (Fig. 6a–d). Seismic reflection profiles and balanced geologi-
367 cal cross-sections depict this as a fault-propagation fold, with Paleozoic-Mesozoic sediments thrust
368 over Cenozoic strata along the moderately northward-dipping Kepingtag fault, which branches off
369 a décollement with an estimated depth of $\sim 5\text{--}10$ km (Yin et al., 1998; Allen et al., 1999; Yang
370 et al., 2010, 2002). Projecting our slip model onto a modified geological cross-section suggests that
371 the 2020 earthquake ruptured the décollement where it intersects with the base of the Kepingtag
372 thrust fault (Fig. 6e).

373 A striking feature of our distributed slip model is its elongate shape, with a width-to-length

374 ratio of less than 1/4 (Figure 4). We interpret that the earthquake was able to propagate read-
375 ily along strike, but was prevented from doing so up- and down-dip. We consider two potential
376 causes of this pattern. One possibility is that the stratigraphic configuration could have determined
377 where slip was able to propagate, with rupture restricted to competent rocks such as the lowermost
378 Cambrian limestone. A similar explanation was proposed by Elliott et al. (2015) for the elongate
379 slip distribution of the 2013 M_w 6.2 Khaki-Shonbe earthquake in the Zagros fold-and-thrust
380 belt, where Infracambrian Hormuz evaporites and Cretaceous Kazhdumi mudstones were inferred
381 to have controlled the bottom and top of the rupture, respectively. Another possible mechanism
382 could be due to structural complexities in the fault geometry. This was discussed by Elliott et al.
383 (2011) for the 2008 and 2009 Qaidam M_w 6.3 earthquakes, whose vertical segregation resulted
384 from disruption of the rupture plane by a cross-cutting, conjugate reverse fault. In the 2020 Jiashi
385 event, we suggest that the abrupt change in dip angle between the sub-horizontal décollement and
386 the much steeper Kepingtag fault may have provided a barrier to rupture. Our testing of listric fault
387 geometries is in good agreement with the inference that there was minimal slip on the steeper fault.
388 Although the current data does not allow us to distinguish between the two mechanisms, there is a
389 clear structural or lithological control on the extent of coseismic slip during the mainshock.

390 **5.3 Regional distribution of seismicity and seismic hazard**

391 The Pamir and Tian Shan jointly accommodate a crustal shortening of 20–25 mm/yr, nearly half
392 of the total India-Eurasia convergence rate (Abdrakhmatov et al., 1996; Zubovich et al., 2010).
393 The southwestern margin of the Tian Shan is characterized by frequent seismicity, mostly with
394 thrust faulting and strike-slip mechanisms. Here, we use our own calibrated earthquake reloca-
395 tions together with previous waveform modelling studies to assess the finer-scale distribution of
396 seismicity across this region.

397 From the calibrated earthquake relocations, it is apparent that seismicity is not concentrated
398 along the frontal Kepingtag belt, but is distributed throughout the fold-and-thrust belt as well as
399 the adjacent foreland to the south. The shallow events occur to the north of the frontal Kepingtag
400 anticline as well as in the foreland to the south. This pattern indicates that the stacking of thrust

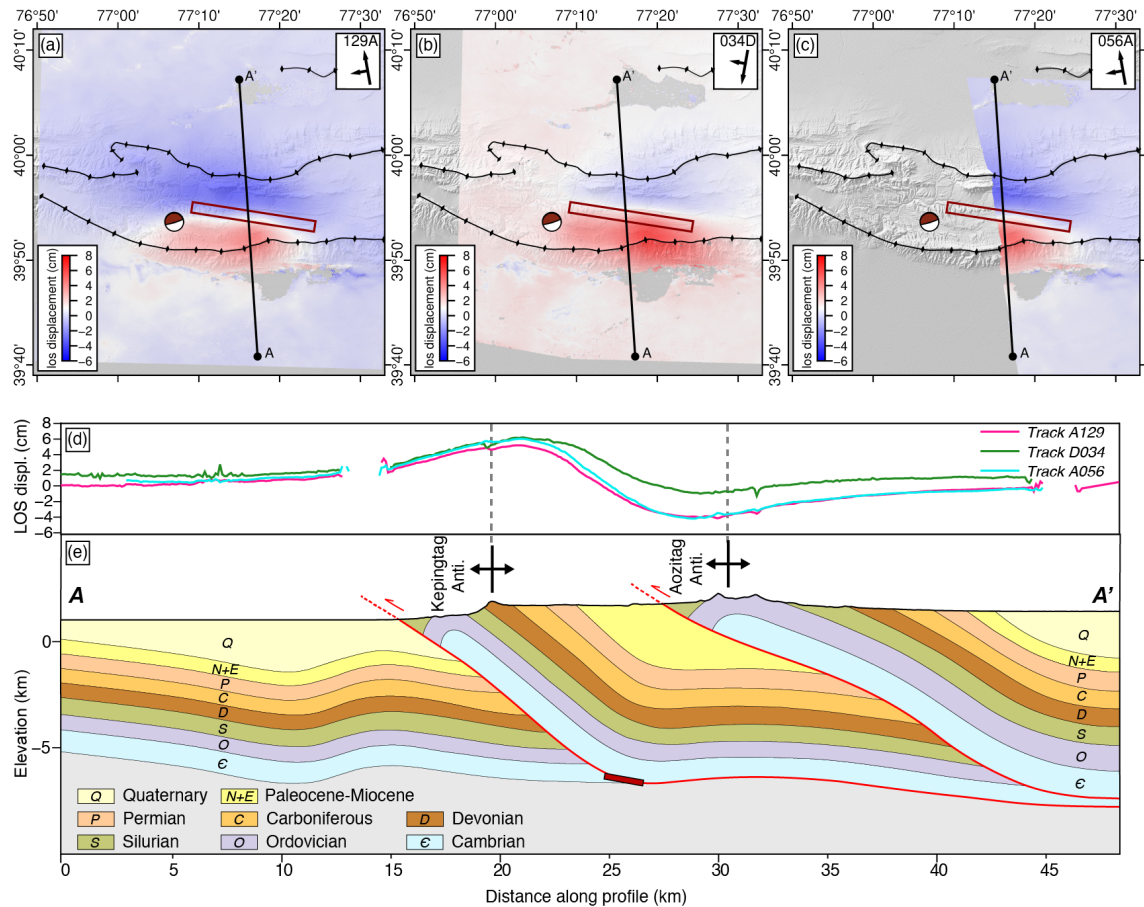


Figure 6. Coseismic LOS displacements in the 2020 Jiashi earthquake from unwrapped interferograms on tracks (a) 129A, (b) 034D and (c) 056A. Black lines with ticks show the traces of the Aozitang (north) and Kepingtag (south) fold axes. The dark red rectangle is the uniform slip model fault plane, centered at ~ 7 km depth. (d) LOS displacement profiles (track 129A in pink, 034D in green, and 056A in cyan) along profile A-A' in (a), (b) and (c). Maximum LOS displacements are ~ 7.5 cm toward the satellite and ~ 4 cm away from the satellite. (e) Geological cross-section along the profile A-A', interpreted from seismic reflection profiles (Yang et al., 2010). The surface topography is extracted from the 30 m resolution SRTM DEM. The dark red rectangle indicates the uniform slip model fault plane.

401 sheets occurs out-of-sequence and the propagation of thrusting into the foreland is not a continuous
 402 process, in agreement with geomorphological and geochronological data (Yang et al., 2006). This
 403 suggests that seismic hazard is high across the region, rather than being focused along the range
 404 front as it is in some other fold-and-thrust belts (e.g., Nissen et al., 2010).

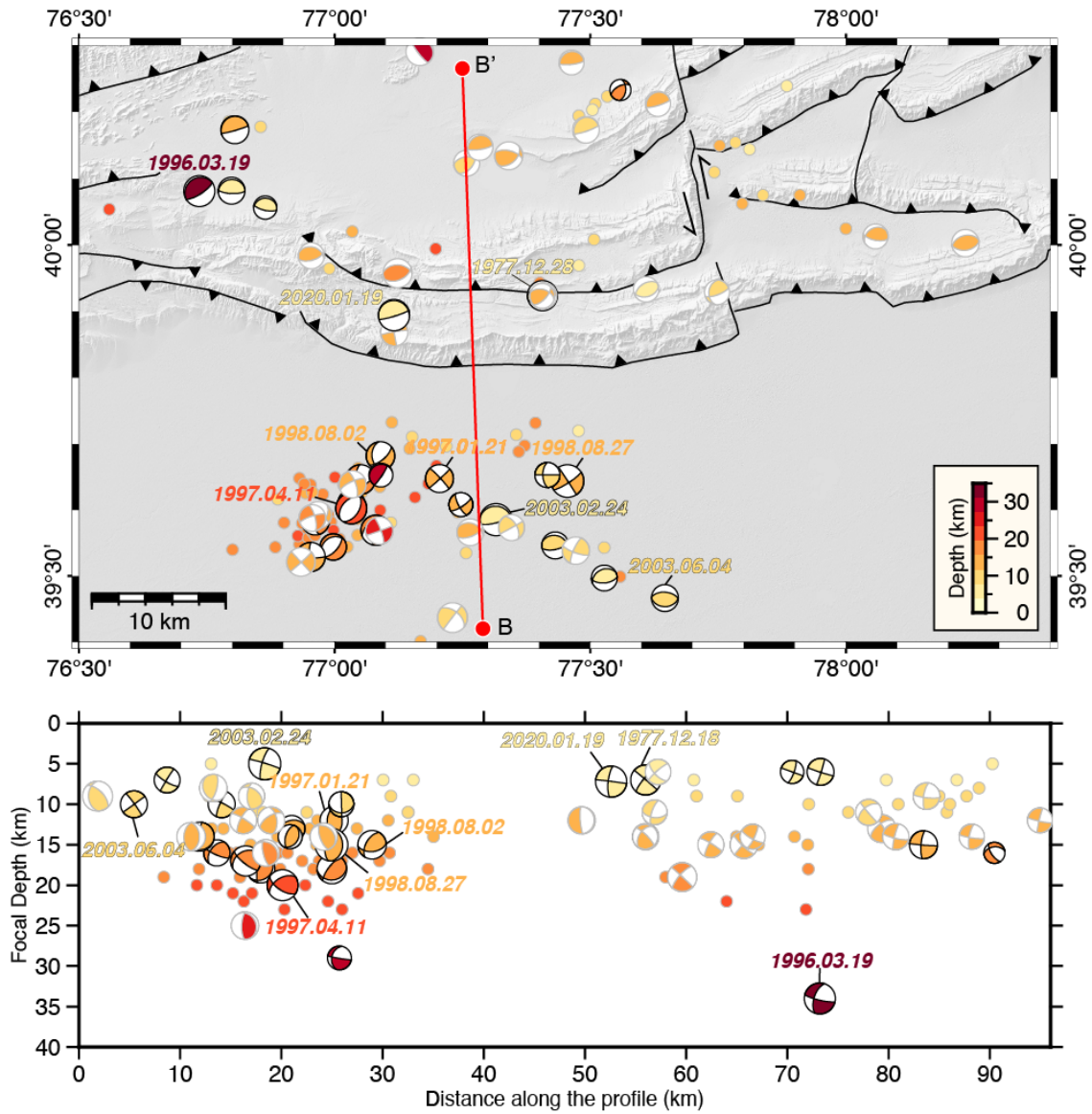


Figure 7. Calibrated relocated earthquakes from 1977–2020 in the Jiashi area, coloured according to the best available estimate of depth. Focal mechanisms determined by teleseismic and regional waveform modelling, including some from the GCMT catalogue. The depths of focal mechanisms with black outlines are determined by teleseismic and regional waveform modelling and depth phases, while those with grey outlines are our own calibrated focal depths (see Table 2 for full details). Other moderate relocated earthquakes without focal mechanisms are shown as dots.

405 Moreover, the seismic hazard in the Kepingtag region is not only restricted to faulting along
406 the décollement but also within the folded and faulted cover rocks. Reliable earthquake centroid
407 and focal depths — from teleseismic or regional waveform modelling (Fan et al., 1994; Ghose
408 et al., 1998; Sloan et al., 2011) and our own calibrated hypocentral relocations — are concentrated
409 at depths shallower than 25 km, except for two isolated events at 29–35 km (Fig. 7). Within the
410 Kepingtag fold-and-thrust belt, most of the reliable centroid depths are greater than 10 km, in-
411 dicating faulting within the basement below the décollement. Though usually depicted as a ‘thin-
412 skinned’ fold-and-thrust belt, the Kepingtag basement clearly accommodates shortening by reverse
413 faulting, and should therefore be considered as an important source of seismic hazard.

414 **6 CONCLUSION**

415 We use InSAR data to characterize the coseismic surface deformation and model the fault geom-
416 etry and slip distribution of the January 19 2020 M_w 6.0 Jiashi earthquake. Modelled coseismic
417 uplift is centered on the back limb of the Kepingtag anticline, consistent with previous structural
418 models that depict this as a fault-propagation fold. Our best-fit model fault plane dips $\sim 7^\circ$ north-
419 ward at depth of ~ 7 km, placing it on or close to the mapped décollement at the base of the folded
420 sedimentary cover. This depth is consistent with teleseismic body-waveforms, confirming that the
421 slip modelled with InSAR occurred coseismically. Published seismological studies show that af-
422 tershocks cluster within underlying basement rocks at ~ 10 – 20 km depth, and we suggest that the
423 absence of shallower aftershocks may reflect that sedimentary layers above the décollement are ve-
424 locity strengthening. Another noticeable feature of the mainshock is its small ratio (1/4) of rupture
425 width to length, which likely reflects structural and/or lithological controls on slip propagation.
426 Specifically, we suggest that slip was prevented from advancing up-dip by the abrupt change of
427 dip angle between the sub-horizontal décollement and the much steeper Kepingtag thrust. Cali-
428 brated earthquake relocations indicate diffuse seismicity across the Kepingtag belt and its adjacent
429 foreland and though the commonly described ‘thin-skinned’ fold-and-thrust belt; most of the reli-
430 able earthquake depths are consistent with locations of faulting in the basement.

431 **ACKNOWLEDGMENTS**

432 S. W. was supported by the China Scholarship Council and a Graduate Award from University of
433 Victoria. E. N. and R. J. were funded separately by the Natural Science and Engineering Research
434 Council of Canada (NSERC), the Canada Foundation for Innovation (CFI) and the BC Knowledge
435 Develoment Fund (BCKDF). E. N. also acknowledges support from a Canada Research Chair.

436 **Data availability**

437 Interferograms were constructed using Copernicus Sentinel-1 data (2020) available from <https://scihub.coperni>
438 and processed in GAMMA software (<https://www.gamma-rs.ch/>). InSAR modelling codes are
439 available from E. N. upon reasonable request. Earthquakes were relocated using *Mloc* software
440 (<https://seismo.com/mloc/>), using starting location parameters from the International Seismolog-
441 ical Centre Bulletin (<http://www.isc.ac.uk/iscbulletin/>). Full calibrated relocation results will be
442 posted to the USGS ScienceBase website for the Global Catalog of Calibrated Earthquake Lo-
443 cations (GCCEL) (<https://www.sciencebase.gov/catalog/item/59fb91fde4b0531197b16ac7>). We
444 also used focal mechanism data from the Global Centroid Moment Tensor project (<https://www.globalcmt.org/>)
445 Several of the figures in the paper were plotted using Generic Mapping Tools (<https://www.generic->
446 [mapping-tools.org/](https://www.generic-mapping-tools.org/)).

447 **References**

- 448 Abdрахmatov, K. Y., Aldazhanov, S. A., Hager, B. H., Hamburger, M. W., Herring, T. A., Kal-
449 abaev, K. B., Makarov, V. I., Molnar, P., Panasyuk, S. V., Prilepin, M. T., Reilinger, R. E.,
450 Sadybakasov, I. S., Souter, B. J., Trapeznikov, Y. A., Tsurkov, V. Y., & Zubovich, A. V., 1996.
451 Relatively recent construction of the Tien Shan inferred from GPS measurements of present-day
452 crustal deformation rates, *Nature*, **384**(6608), 450–453.
- 453 Ainscoe, E. A., Elliott, J. R., Copley, A., Craig, T. J., Li, T., Parsons, B. E., & Walker, R. T., 2017.
454 Blind Thrusting, Surface Folding, and the Development of Geological Structure in the Mw 6.3

- 455 2015 Pishan (China) Earthquake, *Journal of Geophysical Research: Solid Earth*, **122**(11), 9359–
456 9382.
- 457 Allen, M. B., Vincent, S. J., & Wheeler, P. J., 1999. Late Cenozoic tectonics of the Kepingtage
458 thrust zone: Interactions of the Tien Shan and Tarim Basin, northwest China, *Tectonics*, **18**(4),
459 639–654.
- 460 Avouac, J. P. & Tapponnier, P., 1993. Kinematic model of active deformation in central Asia,
461 *Geophysical Research Letters*, **20**(10)(10), 895–898.
- 462 Bergman, E. A., Benz, H. M., Yeck, W. L., Karasözen, E., Engdahl, E. R., Ghods, A., Hayes, G. P.,
463 & Earle, P. S., submitted. A Global Catalog of Calibrated Earthquake Locations, *Geophysical*
464 *Journal International*.
- 465 Burchfiel, B. C., Brown, E. T., Qidong, D., Xianyue, F., Jun, L., Molnar, P., Jianbang, S., Zhang-
466 ming, W., & Huichuan, Y., 1999. Crustal shortening on the margins of the tien shan, Xinjiang,
467 China, *International Geology Review*, **41**(8), 665–700.
- 468 Chen, J., Ran, Y., Yang, X., & Xu, X., 2006. Character of Late Quaternary activity of the east
469 segment of the front-edge faults of Kalpintag, *Seismology and Geology*, **28**(2), 258–268 (in
470 Chinese with English abstract).
- 471 Copley, A., 2014. Postseismic afterslip 30 years after the 1978 Tabas-e-Golshan (Iran) earth-
472 quake: observations and implications for the geological evolution of thrust belts, *Geophysical*
473 *Journal International*, **197**(2), 665–679.
- 474 Copley, A., Karasozen, E., Oveisi, B., Elliott, J. R., Samsonov, S., & Nissen, E., 2015. Seis-
475 mogenic faulting of the sedimentary sequence and laterally variable material properties in the
476 Zagros Mountains (Iran) revealed by the August 2014 Murmuri (E. Dehloran) earthquake se-
477 quence, *Geophysical Journal International*, **203**(2), 1436–1459.
- 478 Davis, T. L., Namson, J., & Yerkes, R. F., 1989. A cross section of the Los Angeles area: seismi-
479 cally active fold and thrust belt, the 1987 Whittier Narrows earthquake, and earthquake hazard,
480 *Journal of Geophysical Research*, **94**(B7), 9644–9664.
- 481 Elliott, J. R., Parsons, B., Jackson, J. A., Shan, X., Sloan, R. A., & Walker, R. T., 2011. Depth
482 segmentation of the seismogenic continental crust: The 2008 and 2009 Qaidam earthquakes,

- 483 *Geophysical Research Letters*, **38**(6), 1–6.
- 484 Elliott, J. R., Bergman, E. A., Copley, A. C., Ghods, A. R., Nissen, E. K., Oveisi, B., Tatar, M.,
485 Walters, R. J., & Yamini-Fard, F., 2015. The 2013 Mw 6.2 Khaki-Shonbe (Iran) Earthquake:
486 Insights into seismic and aseismic shortening of the Zagros sedimentary cover, *Earth and Space*
487 *Science*, **2**(11), 435–471.
- 488 Elliott, J. R., Walters, R. J., & Wright, T. J., 2016. The role of space-based observation in un-
489 derstanding and responding to active tectonics and earthquakes, *Nature Communications*, **7**,
490 13844.
- 491 Engdahl, R. E., Jackson, J. A., Myers, S. C., Bergman, E. A., & Priestley, K., 2006. Relocation
492 and assessment of seismicity in the Iran region, *Geophysical Journal International*, **167**(2),
493 761–778.
- 494 Fan, G., Ni, J. F., & Wallace, T. C., 1994. Active tectonics of the Pamirs and Karakorum, *Journal*
495 *of Geophysical Research*, **99**(B4), 7131.
- 496 Funning, G. J., Parsons, B., Wright, T. J., Jackson, J. A., & Fielding, E. J., 2005. Surface displace-
497 ments and source parameters of the 2003 Bam (Iran) earthquake from Envisat advanced syn-
498 thetic aperture radar imagery, *Journal of Geophysical Research: Solid Earth*, **110**(B9), B09406.
- 499 Gaherty, J. B., Zheng, W., Shillington, D. J., Pritchard, M. E., Henderson, S. T., Chindandali,
500 P. R., Mdala, H., Shuler, A., Lindsey, N., Oliva, S. J., Nooner, S., Scholz, C. A., Schaff, D.,
501 Ekström, G., & Nettles, M., 2019. Faulting processes during early-stage rifting: Seismic and
502 geodetic analysis of the 2009-2010 Northern Malawi earthquake sequence, *Geophysical Journal*
503 *International*, **217**(3), 1767–1782.
- 504 Gaudreau, É., Nissen, E., Bergman, E. A., Benz, H. M., Tan, F., & Karasözen, E., 2019. The Au-
505 gust 2018 Kaktovik earthquakes: Active tectonics in northeastern Alaska revealed with InSAR
506 and seismology, *Geophysical Research Letters*, **46**(24), 14412–14420.
- 507 Ghose, S., Hamburger, M. W., & Ammon, C. J., 1998. Source parameters of moderate-sized
508 earthquakes in the Tien Shan, central Asia from regional moment tensor inversion, *Geophysical*
509 *Research Letters*, **25**(16), 3181–3184.
- 510 Goldstein, R. M., Zebker, H. A., & Werner, C. L., 1988. Satellite radar interferometry: Two-

- 511 dimensional phase unwrapping, *Radio Science*, **23**(4), 713–720.
- 512 Gomberg, J. S., Shedlock, K. M., & Roecker, S. W., 1990. The effect of S-wave arrival times
513 on the accuracy of hypocenter estimation, *Bulletin of the Seismological Society of America*,
514 **80**(6A), 1605–1628.
- 515 Heimann, S., Isken, M., Kühn, D., Sudhaus, H., Steinberg, A., Daout, S., Cesca, S., Bathke, H.,
516 & Dahm, T., 2018. Grond: A probabilistic earthquake source inversion framework.
- 517 Hendrix, M. S., Graham, S. A., Carroll, A. R., Sobel, E. R., McKnight, C. L., Schulein, B. J., &
518 Wang, Z., 1992. Sedimentary record and climatic implications of recurrent deformation in the
519 Tian Shan: evidence from Mesozoic strata of the north Tarim, south Junggar, and Turpan basins,
520 northwest China, *Geological Society of America Bulletin*, **104**(1), 53–79.
- 521 Huang, Y., Yang, J. S., & Zhang, T. Z., 2006. Relocation of the Bachu-Jiashi, Xinjiang earthquake
522 sequence in 2003 using the double-difference location algorithm, *Acta Geophysica Sinica*,
523 **49**(1), 162–169.
- 524 Jackson, J., Bouchon, M., Fielding, E., Funning, G., Ghorashi, M., Hatzfeld, D., Nazari, H., Par-
525 sons, B., Priestley, K., Talebian, M., Tatar, M., Walker, R., & Wright, T., 2006. Seismotectonic,
526 rupture process, and earthquake-hazard aspects of the 2003 December 26 Bam, Iran, earthquake,
527 *Geophysical Journal International*, **166**(3), 1270–1292.
- 528 Jones, L., Aki, K., Boore, D., Celebi, M., Donnellan, A., Hall, J., Harris, R., Hauksson, E.,
529 Heaton, T., Hough, S., Hudnut, K., Hutton, K., Johnston, M., Joyner, W., Kanamori, H., Mar-
530 shall, G., Michael, A., Mori, J., Murray, M., Ponti, D., Reasenber, P., Schwartz, D., Seeber,
531 L., Shakal, A., Simpson, R., Thio, H., Tinsley, J., Todorovska, M., Trifunac, M., Wald, D., &
532 Zoback, M. L., 1994. The magnitude 6.7 Northridge, California, earthquake of 17 January 1994,
533 *Science*, **266**(5184), 389–397.
- 534 Jónsson, S., Zebker, H., Segall, P., & Amelung, F., 2002. Fault slip distribution of the 1999 Mw
535 7.1 Hector Mine, California, earthquake, estimated from satellite radar and GPS measurements,
536 *Bulletin of the Seismological Society of America*, **92**(4), 1377–1389.
- 537 Jordan, T. H. & Sverdrup, K. A., 1981. Teleseismic location techniques and their application to
538 earthquake clusters in the South-Central Pacific, *Bulletin of the Seismological Society of Amer-*

539 *ica*, **71**, 1105–1130.

540 Karasözen, E., Nissen, E., Bergman, E. A., Johnson, K. L., & Walters, R. J., 2016. Normal fault-
541 ing in the Simav graben of western Turkey reassessed with calibrated earthquake relocations,
542 *Journal of Geophysical Research: Solid Earth*, **121**(6), 4553–4574.

543 Karasözen, E., Nissen, E., Büyükakpınar, P., Cambaz, M. D., Kahraman, M., Kalkanâ Ertan,
544 E., Abgarmi, B., Bergman, E., Ghods, A., & Özacar, A. A., 2018. The 2017 July 20 M_w 6.6
545 Bodrum-Kos earthquake illuminates active faulting in the Gulf of Gökova, SW Turkey, *Geo-*
546 *physical Journal International*, **214**(1), 185–199.

547 Karasözen, E., Nissen, E., Bergman, E. A., & Ghods, A., 2019. Seismotectonics of the Za-
548 gros (Iran) From Orogen-Wide, Calibrated Earthquake Relocations, *Journal of Geophysical Re-*
549 *search: Solid Earth*, **124**(8), 9109–9129.

550 Kulikova, G. & Krüger, F., 2017. Historical seismogram reproductions for the source parameters
551 determination of the 1902, Atushi (Kashgar) earthquake, *Journal of Seismology*, **21**(6), 1577–
552 1597.

553 Mallick, R., Bürgmann, R., Johnson, K., & Hubbard, J., 2021. A unified framework for earth-
554 quake sequences and the growth of geological structure in fold-thrust belts, *Journal of Geophys-*
555 *ical Research: Solid Earth*.

556 Nishidai, T. & Berry, J. L., 1990. Structure and Hydrocarbon Potential of the Tarim Basin (Nw
557 China) From Satellite Imagery, *Journal of Petroleum Geology*, **13**(1), 35–58.

558 Nissen, E., Yamini-Fard, F., Tatar, M., Gholamzadeh, A., Bergman, E., Elliott, J. R., Jackson,
559 J. A., & Parsons, B., 2010. The vertical separation of mainshock rupture and microseismicity
560 at Qeshm island in the Zagros fold-and-thrust belt, Iran, *Earth and Planetary Science Letters*,
561 **296**(3-4), 181–194.

562 Nissen, E., Tatar, M., Jackson, J. A., & Allen, M. B., 2011. New views on earthquake faulting in
563 the Zagros fold-and-thrust belt of Iran, *Geophysical Journal International*, **186**(3), 928–944.

564 Nissen, E., Jackson, J., Jahani, S., & Tatar, M., 2014. Zagros "phantom earthquakes" reassessed -
565 The interplay of seismicity and deep salt flow in the Simply Folded Belt?, *Journal of Geophys-*
566 *ical Research: Solid Earth*, **119**(4), 3561–3583.

- 567 Okada, Y., 1992. Internal deformation due to shear and tensile faults in a half-space, *Bulletin -*
568 *Seismological Society of America*, **82**(2), 1018–1040.
- 569 Pousse-Beltran, L., Nissen, E., Bergman, E. A., Cambaz, M. D., Gaudreau, É., Karasözen, E., &
570 Tan, F., 2020. The 2020 M_w 6.8 Elazığ (Turkey) Earthquake Reveals Rupture Behavior of the
571 East Anatolian Fault, *Geophys. Res. Lett.*, , **47**(13), e88136.
- 572 Press, W. H., Flannery, B. P., Teukolsky, S. A., & Vetterling, W. T., 1992. Numeric recipes in C:
573 the art of scientific computing, *Camb. Univ. Press Camb.*
- 574 Ran, H., Shanguan, W., & Liu, D., 2020. Location study of Xinjiang Jiashi Ms6.4 earthquake
575 and aftershocks sequence on January 19th, 2020, *Inland Earthquake*, **34**(1), 56–61.
- 576 Ran, Y., Yang, X., Xu, X., Cheng, J., & Chen, L., 2006. Deformation pattern and shortening
577 rates in the east part of Kalpin Thrust system in southwest Tianshan during late Quaternary,
578 *Seismology and Geology (in Chinese with English abstract)*, **28**(2), 179–193.
- 579 Reigber, C., Michel, G. W., Galas, R., Angermann, D., Klotz, J., Chen, J. Y., Papschev, A., Ar-
580 slanov, R., Tzurkov, V. E., & Ishanov, M. C., 2001. New space geodetic constraints on the
581 distribution of deformation in Central Asia, *Earth and Planetary Science Letters*, **191**(1-2),
582 157–165.
- 583 Roustaei, M., Nissen, E., Abbassi, M., Gholamzadeh, A., Ghorashi, M., Tatar, M., Yamini-Fard,
584 F., Bergman, E., Jackson, J., & Parsons, B., 2010. The 2006 March 25 Fin earthquakes (Iran)-
585 insights into the vertical extents of faulting in the Zagros Simply Folded Belt, *Geophysical*
586 *Journal International*, **181**(3), 1275–1291.
- 587 Semmane, F., Cotton, F., & Campillo, M., 2005. The 2000 Tottori earthquake: A shallow earth-
588 quake with no surface rupture and slip properties controlled by depth, *Journal of Geophysical*
589 *Research: Solid Earth*, **110**(3), 1–13.
- 590 Sloan, R. A., Jackson, J. A., Mckenzie, D., & Priestley, K., 2011. Earthquake depth distribu-
591 tions in central Asia, and their relations with lithosphere thickness, shortening and extension,
592 *Geophysical Journal International*, **185**(1), 1–29.
- 593 Tong, X., Sandwell, D. T., & Fialko, Y., 2010. Coseismic slip model of the 2008 Wenchuan
594 earthquake derived from joint inversion of interferometric synthetic aperture radar, GPS, and

- 595 field data, *Journal of Geophysical Research*, **115**(B4), 1–19.
- 596 Walker, R., Jackson, J., & Baker, C., 2003. Surface expression of thrust faulting in eastern Iran:
597 source parameters and surface deformation of the 1978 Tabas and 1968 Ferdows earthquake
598 sequences, *Geophysical Journal International*, **152**(3), 749–765.
- 599 Walker, R. T., Bergman, E. A., Szeliga, W., & Fielding, E. J., 2011. Insights into the 1968-
600 1997 Dasht-e-Bayaz and Zirkuh earthquake sequences, eastern Iran, from calibrated relocations,
601 InSAR and high-resolution satellite imagery, *Geophysical Journal International*, **187**(3), 1577–
602 1603.
- 603 Wang, D., Zhao, B., Yu, J., & Tan, K., 2020. Active tectonic deformation around the Tarim Basin
604 inferred from dense GPS measurements, *Geodesy and Geodynamics*, **11**(6), 418–425.
- 605 Wei, S., Barbot, S., Graves, R., Lienkaemper, J. J., Wang, T., Hudnut, K., Fu, Y., & Helmberger,
606 D., 2015. The 2014 Mw 6.1 South Napa Earthquake: A unilateral rupture with shallow asperity
607 and rapid afterslip, *Seismological Research Letters*, **86**(2A), 344–354.
- 608 Weston, J., Ferreira, A. M. G., & Funning, G. J., 2011. Global compilation of interferometric syn-
609 thetic aperture radar earthquake source models: 1. Comparisons with seismic catalogs, *Journal*
610 *of Geophysical Research: Solid Earth*, **116**(B8), B08408.
- 611 Wimpenny, S. & Scott Watson, C., 2020. gWFM: A global catalog of moderate-magnitude earth-
612 quakes studied using teleseismic body waves, *Seismological Research Letters*, **92**(1), 212–226.
- 613 Windley, B. F., Allen, M. B., Zhang, C., Zhao, Z. Y., & Wang, G. R., 1990. Paleozoic accretion
614 and Cenozoic redeformation of the Chinese Tien Shan Range, central Asia.
- 615 Wright, T. J., Parsons, B. E., Jackson, J. A., Haynes, M., Fielding, E. J., England, P. C., & Clarke,
616 P. J., 1999. Source parameters of the 1 October 1995 Dinar (Turkey) earthquake from SAR
617 interferometry and seismic bodywave modelling, *Earth and Planetary Science Letters*, **172**(1-
618 2), 23–37.
- 619 Wright, T. J., Lu, Z., & Wicks, C., 2004. Constraining the slip distribution and fault geometry of
620 the Mw 7.9, 3 November 2002, Denali fault earthquake with Interferometric Synthetic Aperture
621 Radar and Global Positioning System data, *Bulletin of the Seismological Society of America*,
622 **94**(6 SUPPL. B), 175–189.

- 623 Xu, Y., Roecker, S. W., Wei, R., Zhang, W., & Wei, B., 2006. Analysis of seismic activity in the
624 crust from earthquake relocation in the central Tien Shan, *Bulletin of the Seismological Society*
625 *of America*, **96**(2), 737–744.
- 626 Yang, H., Li, Y., Shi, J., Xiao, A., Huang, S., Wu, G., Wang, H., Wang, X., Zhao, Y., & Liu,
627 Y., 2010. Tectonic characteristics of the Late Cenozoic south Tianshan fold-and-thrust belt,
628 *Quaternary Sciences*, **30**(5), 1030–1043 (in Chinese with English abstract).
- 629 Yang, X., Ran, Y., Song, F., Xu, X., Cheng, J., Min, W., Han, Z., & Chen, L., 2006. The analysis
630 for crust shortening of Kalpin Thrust tectonic zone, south-western Tianshan, Xinjiang, China,
631 *Seismology and Geology (in Chinese with English abstract)*, **28**(2), 194–204.
- 632 Yang, Z. X., Zhao, J. R., Zhang, X. K., Zhang, C. K., Cheng, S. X., Duan, Y. L., Zhang, J. S., &
633 Wang, S. J., 2002. Tomographic determination of the upper crustal structure in the Jiashi strong
634 earthquake swarm region, *Acta Seismologica Sinica English Edition*, **15**(2), 162–170.
- 635 Yao, Q., Yang, W., Jiang, X., Guo, Y., Liu, J., Zhang, Y., Wang, H., Ren, J., Yu, C., Yue, C.,
636 & Zhao, J., 2021a. The 2020 M6.4 Jiashi Earthquake: An Event that Occurred Under the
637 Décollement on the Kaping Fold-and-Thrust Belt in the Southwestern Tien Shan Mountains,
638 China, *Frontiers in Earth Science*, **9**(May), 1–14.
- 639 Yao, Y., Wen, S., Li, T., & Wang, C., 2021b. The 2020 Mw6.0 Jiashi earthquake: A fold earth-
640 quake event in the southern Tian Shan, northwest China, *Seismological Research Letters*, **92**(2),
641 859–869.
- 642 Yin, A., Craig, P., Harrison, T. M., Ryerson, F. J., Qian, X., & Yang, G., 1998. Late Cenozoic
643 tectonic evolution of the southern Chinese Tian Shan, *Tectonics*, **17**(1), 1–27.
- 644 Yu, P., Qiao, X., Xiong, W., Chen, W., Nie, Z., Wang, D., Jia, Z., & Li, J., 2020. Source model
645 for the M w 6.0 earthquake in Jiashi, China on 19 January 2020 from Sentinel-1A InSAR data,
646 *Earth, Planets and Space*, **72**(1).
- 647 Zhang, G., Zhu, L., Song, X., Li, Z., Yang, M., Su, N., & Chen, X., 1999. Predictions of the 1997
648 strong earthquakes in Jiashi, Xinjiang, China, *Bulletin of the Seismological Society of America*,
649 **89**(5), 1171–1183.
- 650 Zhang, Z. Q., Chen, J. Y. S., & Lin, J., 2008. Stress interactions between normal faults and

651 adjacent strike-slip faults of 1997 Jiashi earthquake swarm, *Science in China, Series D: Earth*
652 *Sciences*, **51**(3), 431–440.

653 Zhou, S. Y. & Xu, Z. H., 2000. Fracture characteristics of the 1997 Jiashi, Xinjiang, China, earth-
654 quake swarm inferred from source spectra, *Acta Seismologica Sinica English Edition*, **13**(2),
655 125–135.

656 Zubovich, A. V., Wang, X. Q., Scherba, Y. G., Schelochkov, G. G., Reilinger, R., Reigber, C.,
657 Mosienko, O. I., Molnar, P., Michajljow, W., Makarov, V. I., Li, J., Kuzikov, S. I., Herring,
658 T. A., Hamburger, M. W., Hager, B. H., Dang, Y. M., Bragin, V. D., & Beisenbaev, R. T., 2010.
659 GPS velocity field for the Tien Shan and surrounding regions, *Tectonics*, **29**(6), 1–23.